A Novel Algorithm for Sprial Large FOV Reconstruction

Dalong Tan, Xin Tian, Yixin He, Chenhao Xu, Kaisheng Li, and Min Yang*

School of Mechanical Engineering and Automation, Beihang University, 100191, Beijing, China Email: dalong_edu@163.com (D.T.); tianx@buaa.edu.cn (X.T.); 1961775390@qq.com (Y.H.); xuchenhao0925@163.com (C.X.); q2098377686@163.com (K.L.); minyang.ndt@buaa.edu.cn (M.Y.) *Corresponding author

Abstract—Cone-beam spiral Computed Tomography (CT) naturally extends longitudinal coverage, yet its transverse Field of View (FOV) remains constrained, causing projection truncation at high geometric magnification. We present an offset-spiral acquisition scheme paired Parker-weighted reconstruction algorithm that doubles the usable transverse FOV without modifying hardware. The one-sided lateral shift introduces projection redundancy, which is compensated by a tailored weighting function, allowing accurate recovery of truncated data through the standard Feldkamp-Davis-Kress (FDK) pipeline. Tests on simulated phantoms and real lithium-battery scans show that the proposed method preserves fine structural details and attains image quality comparable to conventional full-FOV (mean PSNR \approx 32 dB, reconstructions SSIM ≈ 0.99 . MSE < 0.014, FSIM and VIF<0.97). The technique is readily deployable in existing industrial CT systems and broadens the applicability of spiral FDK reconstruction to large, high-aspect-ratio objects.

Keywords—industrial CT, spiral FDK, unilateral truncation, lithium battery, Parker weights

I. INTRODUCTION

In the field of industrial and medical Computed Tomography (CT), the spatial resolution of an image represents the ability of the CT device to distinguish the smallest size of objects. If the spatial resolution of the imaging device is insufficient, it will not be able to produce clear and high-quality imaging of small structures within the object. Factors that determine the spatial resolution of an image include the pixel size of the detector, the focal size of the X-ray source, and the imaging magnification ratio. The pixel size determines the spatial sampling capability of the detector, and smaller pixel sizes can provide higher spatial resolution, allowing for better capture of fine details. The focal size of the X-ray source determines the focusing ability of the X-ray beam, and smaller focal size can concentrate the X-ray beam more, thereby improving spatial resolution [1, 2]. The imaging magnification ratio refers to the proportional relationship between the size of objects in the image and their actual

size. A higher imaging magnification ratio can magnify the details in the image, thus improving spatial resolution. In practical imaging, the detector and X-ray source are already determined, and the corresponding pixel size and focal size cannot be changed. Therefore, higher resolution imaging can only be achieved by changing the imaging magnification ratio.

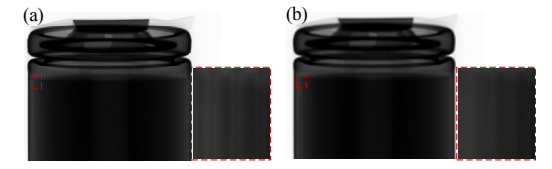


Fig. 1. Slice images of lithium batteries with different magnification ratios: (a) Magnification ratio is 6.129; (b) The amplification ratio is 2.112

From Fig. 1, it can be observed that increasing the magnification ratio leads to higher resolution images. However, once the model of the detector is determined, its corresponding imaging Field of View becomes limited. As the magnification ratio increases, the limited FOV is unable to capture the complete image of the object under inspection. As shown in Fig. 2, under high magnification conditions, the detector can only perform partial sampling of the test object.

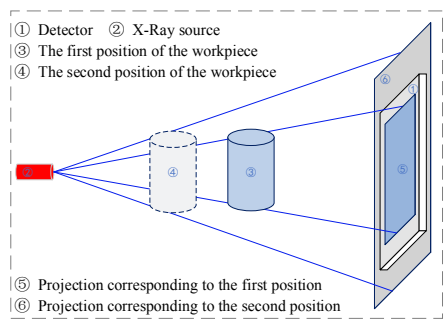


Fig. 2. The limited FOV of detectors under high magnification ratio.

II. RELATED THEORY

The purpose of this article is to design a Large FOV (LFOV) algorithm based on the spiral Feldkamp-Davis-

Manuscript received June 9, 2025; revised June 16, 2025; accepted July 31, 2025; published November 25, 2025.

doi: 10.18178/joig.13.6.637-644 637

Kress (FDK) theory. To gain a deep understanding of the proposed algorithm, this section will first conduct an indepth analysis of the Filtered Back Projection (FBP) algorithm. As the foundation of image reconstruction, the FBP algorithm provides a key understanding of the fundamental reconstruction principles and is a prerequisite for understanding more advanced reconstruction algorithms. Building upon the FBP algorithm, the study of the basic theory of circular trajectory FDK represents an important transition from two-dimensional to three-dimensional reconstruction. The analysis of the circular trajectory FDK algorithm can provide important theoretical support for understanding the spiral FDK algorithm. Finally, this section introduces the principles of the spiral FDK reconstruction algorithm.

The introduction of cone-beam X-ray source and flatpanel detector has brought significant changes to the field of CT. Compared to traditional fan-beam sources, conebeam sources demonstrate superior performance in terms of radiation utilization efficiency and image acquisition, effectively reducing radiation dose while also improving image reconstruction speed. In addition, the application of three-dimensional reconstruction techniques allows for obtaining higher precision volumetric data, overcoming the limitations of traditional two-dimensional reconstruction methods in longitudinal resolution.

The FDK algorithm is a reconstruction method designed specifically for cone-beam circular trajectory scanning, providing an efficient and approximate solution. This algorithm is known for its simplicity and fast processing capabilities, and has become one of the most widely used techniques in modern industrial CT applications, especially in the field of 3D filtered back projection reconstruction [3]. For cone-beam CT, the key of the FDK algorithm lies in treating the cone-beam source as a superposition of multiple fan-beam sources tilted at different angles, particularly in the central plane (i.e., the plane where the cone angle is zero), where the algorithm's data reconstruction is consistent with the precise reconstruction method for fan-beam scanning. However, when dealing with non-central planes, appropriate adjustments to the fan-beam scanning FBP algorithm are required to obtain approximate reconstruction results [4, 5].

Larger projection magnification ratio is usually required to accurately capture their internal structure when performing CT imaging on long objects. Due to the size limitation of the flat-panel detector in the longitudinal direction, circular trajectory scanning often fails to obtain complete longitudinal projection data of the object. To address this issue, the spiral trajectory scanning method has been designed, which extends the imaging range in the longitudinal direction and allows for the acquisition of complete projection data in a single scan. Reconstruction algorithms for spiral scanning trajectories mainly include analytical algorithms and iterative algorithms, among which analytical algorithms are more commonly used in practical applications. These algorithms include both exact reconstruction and approximate reconstruction methods, and among the approximate reconstruction methods, the FDK algorithm stands out for its clear mathematical

derivation, efficient reconstruction efficiency, good noise resistance, and excellent spatial resolution, making it one of the most commonly used cone-beam CT reconstruction algorithms. The original FDK algorithm is designed for standard circular trajectories, and the spiral FDK algorithm applicable to spiral trajectory reconstruction is developed through subsequent improvements by researchers. The spiral FDK algorithm demonstrates its efficient reconstruction accuracy when dealing with larger cone angles of the X-ray beam [6, 7].

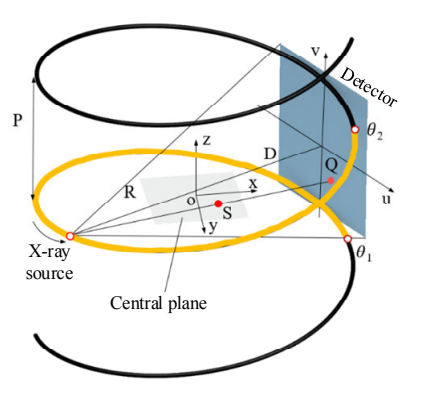


Fig. 3. Schematic diagram of spiral CT.

The scanning system of cone-beam spiral CT is shown in Fig. 3 where R is defined as the radius from the X-ray source to the axis of rotation, D is the distance from the Xray source to the detector, and P is the pitch of the spiral scan. The rotation angle of the X-ray source around the central axis is denoted by θ , and the spiral path of the Xray source can be described by $(R\cos\theta, R\sin\theta, \frac{P\theta}{2\pi})$. As the X-ray source moves from position θ_1 to θ_2 , we can capture data $q(\theta, u_f, v_f)$ of the projection point Q on the flat detector that corresponds to the detected point S(x,y,z). The relationship between these data and the target function f(x, y, z) that needs to be reconstructed can be expressed by formula (1), which is the core of the spiral FDK. In this way, a three-dimensional target function can be reconstructed from a series of two-dimensional projections, providing an effective image reconstruction method for spiral CT scanning [8, 9].

$$\begin{cases} f(x,y,z) = \int_{\theta_{l}}^{\theta_{2}} \frac{R^{2}}{(R - x\cos\theta - y\sin\theta)^{2}} \tilde{p}(\theta, u_{f}, v_{f}) d\theta \\ u_{f} = \frac{D(-x\sin\theta + y\cos\theta)}{R - x\cos\theta - y\sin\theta} \\ v_{f} = \frac{D(z - \frac{P\theta}{2\pi})}{R - x\cos\theta - y\sin\theta} \end{cases}$$
(1)

In Eq. (1), u_f and v_f represent the coordinates during back projection, $\tilde{p}(\theta, u, v)$ denotes the weighted and filtered data obtained from the original projection data.

$$\tilde{p}(\theta, u, v) = \left(\frac{D}{\sqrt{D^2 + u^2 + v^2}} \cdot p(\theta, u, v)\right) \times h(u) \quad (2)$$

III. PROPOSED METHOD

The spiral scanning can effectively solve the problem of longitudinal truncation in imaging of long objects. However, the conventional reconstruction algorithm of spiral FDK cannot effectively address the problem of transverse truncation in imaging under high magnification conditions. Based on the principle of the spiral FDK, it is known that interpolation of projection data within a 180degree range above and below the reconstructed slice is required during the reconstruction of the tomographic image. Then, the circular trajectory FDK reconstruction algorithm and the interpolated projection are used for the reconstruction process. Therefore, this section analyzes the problem of truncated projection reconstruction using the circular trajectory cone-beam scanning geometry as an example and designs a spiral offset scanning scheme without changing the imaging conditions. Corresponding modifications are made to the spiral reconstruction algorithm.

A. The Geometry of Image Acquisition Systems

As shown in Fig. 4(a), S represents the X-ray source, CD represents the detector, Os represents the projected position of the central ray on the detector, MN represents the position of the rotator, O represents the rotation center, and OO_I represents the distance of the rotator's offset. In order to improve the imaging range, the rotator can be offset according to the scheme shown in Fig. 4(b), while ensuring that the imaging FOV can cover at least half of the scanning area.

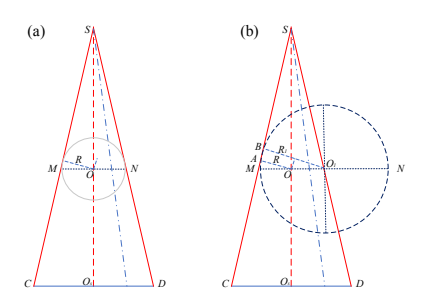


Fig. 4. Comparison between conventional scanning and offset scanning.

As shown in Fig. 4, under the same conditions, the radius of the imaging FOV for the conventional scanning is R. After the rotator is horizontally displaced, the imaging FOV is R_I , where:

$$R_{1} = R + \overline{OO_{1}} \cdot \frac{\overline{SOO_{S}}}{\sqrt{\overline{O_{S}D}^{2} + \overline{SOO_{S}}^{2}}}$$
 (3)

From Eq. (3), it can be concluded that when the rotaror is moved to the position of point M or point N in Fig. 4(a), the imaging FOV reaches its maximum. In Fig. 4(b), ΔMAO and ΔMBO_1 are similar triangles, and $BO_1 = 2MO$, therefore $R_1 = 2R$, thus the maximum imaging FOV can be expanded by a factor of 1.

B. Parker Weights

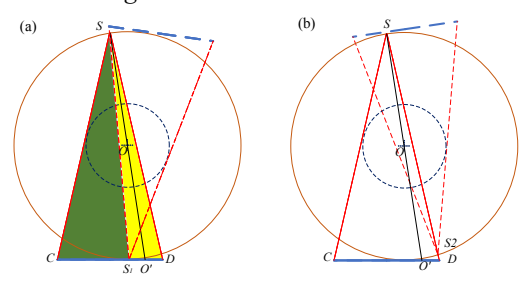


Fig. 5. Diagram of redundant areas in offset scan.

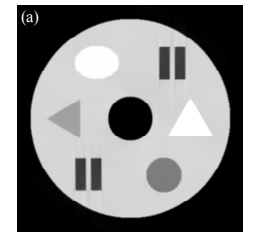
Taking the central plane as an example, for conventional scanning geometry, the entire scanning process involves a 360-degree rotation of the rotator, resulting in the X-ray penetration path being repeated twice. However, for offset scanning, due to the truncation of the projection, only the localized region is within the FOV of the detector at a single projection angle. As shown in Fig. 5, during the 360-degree scanning process, the Δ SCS_1 region is penetrated by the X-ray only once, while the Δ SDS_1 region is penetrated twice. If the collected projections are directly used for reconstruction, the participation of partially repeated projections in the back projection process can lead to image distortion.

To investigate the influence of unilateral truncation of projected images in offset scan on the quality of reconstructed images, a virtual CT imaging experiment is designed to acquire simulated data. The specific parameters are shown in Table I.

TABLE I. MAIN PARAMETERS OF SIMULATION EXPERIMENT

Samples	Projections	Size	FDD (mm)	Magnification ratio	Offset (mm)	Pixel size (mm)
1	720	512×512	1250	1.25	0	0.2
2	720	512×512	1250	1.5625	20	0.2

For the projections generated based on the parameters in Table I, reconstruction is performed using the spiral FDK algorithm, and the reconstructed images are shown in Fig. 6. It can be clearly observed that direct reconstruction of the image using truncated projections allows for the overall contour of the object to be restored, with higher resolution in the foreground region. However, the overall brightness of the image is distorted, and the image details are deformed, with the central region exhibiting a ring artifact.



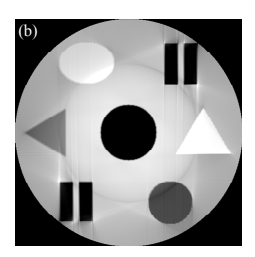


Fig. 6. Comparison of reconstruction results: (a) reconstruction result of complete projections; (b) reconstruction result of unilateral truncated projection.

In the turntable-offset scanning mode, the repeatedly sampled projections can be visualised in a β - θ coordinate system, where the vertical axis represents the rotation angle β and the horizontal axis the fan angle θ , as shown in Fig. 7. The shaded area marks the redundant-projection region. Eq. (6) demonstrates that the Parker weighting makes the summed weights in this redundant region equal to 1 [10].

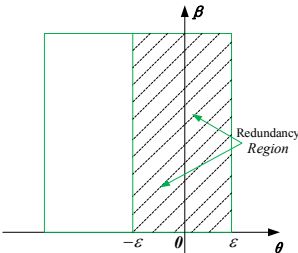


Fig. 7. Illustration of the redundant region in the single-offset turntable mode (where β denotes the rotation angle of the turntable).

$$w(\theta) = \begin{cases} \frac{1}{2} \left(\sin(\frac{\pi \theta}{2\varepsilon}) + 1 \right) & -\varepsilon \le \theta \le \varepsilon \\ 1 & \theta < -\varepsilon \end{cases}$$
 (4)

$$\varepsilon = \theta - \arctan(\frac{\overline{OO_1}}{\overline{SO}}) \tag{5}$$

$$\frac{1}{2} \left(\sin \left(\frac{\pi \theta}{-2\varepsilon} \right) + 1 \right) + \frac{1}{2} \left(\sin \left(\frac{-\pi \theta}{-2\varepsilon} \right) + 1 \right) = 1 \quad (6)$$

As shown in Fig. 7, the symbol ε in formula (4) represents the region of projection redundancy; S represents the ray source; γ represents the angle between other rays and the central ray; θ represents the angle between the ray and SO, where SO is the ray passing through the rotation center; D is the vertical distance between the ray source and the detector. \overline{SO} in formula (5) represents the distance from the X-ray source to the center of the turntable.

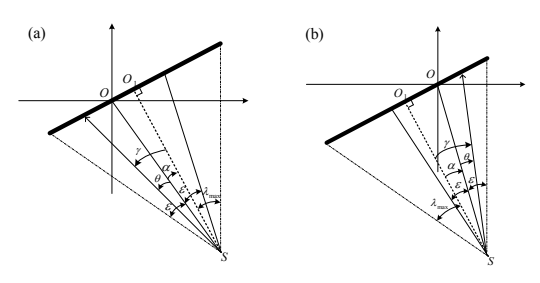


Fig. 8. Schematic diagram of offset scanning geometry: (a) the rotator shifted to the right to the left, (b) the rotator shifted to the right.

The offset direction for Fig. 8 is defined as follows: with the center of the detector as the reference, if the projection position of the rotator on the detector is to the left of the detector' center, the offset direction is leftward; otherwise, it is rightward. From Fig. 8, it can be deduced that, $\theta = \gamma - \alpha$, therefore, $p(\beta, \theta)$ can be expressed as $p(\beta, \gamma)$: when the rotator is shifted to the left: $-\varepsilon \le \rho \le \varepsilon \implies -\lambda_{\max} \le \gamma \le \lambda_{\max} - 2\alpha$, when the rotator is shifted to the right:

 $-\varepsilon \le \rho \le \varepsilon$ \Rightarrow $2\alpha - \lambda_{\max} \le \gamma \le \lambda_{\max}$.

C. Implementation Steps

As mentioned above, for the projection truncation, it is necessary to use the designed Parker function to weight the original projections, and then use the spiral FDK algorithm to perform back projection on the weighted projection images to complete the image reconstruction. The following is the workflow for spiral FDK reconstruction of unilateral truncation projections:

- 1) Determine the offset distance of the rotator.
- 2) Expand the projection images.

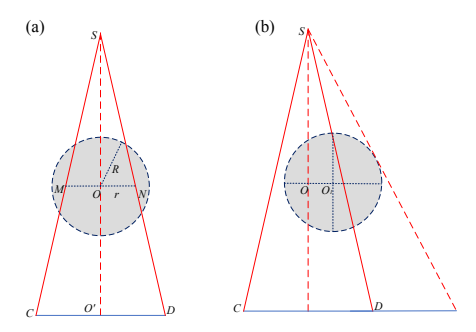


Fig. 9. Illustration of detector extension: (a) the rotator is centered (b) the rotator shifted to the right.

As shown in Fig. 9, it can obtain the complete FOV of the circular region by expanding the detector along the CD direction. The radius of the FOV is denoted as r, and the radius of the circular region is denoted as R. For the imaging position in Fig. 9(a), there are partial regions on both sides of the circular region that are not within the FOV. with a length beyond the FOV denoted as R-r. Offsetting the rotator to the right with an offset distance denoted as offset according to Fig. 9(b), the length beyond the FOV on the right side is R - r + offset. When reconstructing the image, the size of the slice image is determined based on the width of the projection. If the size of the projection image is not modified, the reconstructed image will be truncated which is shown in Fig. 6(b). Therefore, it is necessary to widen the projection image, and the length of the widening can be calculated using formula (5).

$$\begin{cases}
Len = (R - r + offset) \times ratio \\
ratio = \frac{SO'}{SO}
\end{cases}$$
(7)

In formula (7), *Len* represents the length of the projection expansion, while *ratio* denotes the magnification ratio.

- 3) Apply Parker weights to the projection images according to Eq. (4).
- 4) Perform filtering on the weighted images.
- 5) Reconstruct the slices according to Eq. (1).

IV. EXPERIMENTS AND ANALYSIS

A. Experiment of Reconstruction

To verify the performance of the proposed algorithm, this section conducts a controlled experiment. The controlled experiment included simulated data and real lithium battery data. The simulated data are generated

using open-source code (copyright owned by the University of Bath and the European Organization for Nuclear Research: European Nuclear Research

Organization). The specific experimental parameters are shown in Table II.

TABLE II. MAIN EXPERIMENTAL PARAMETERS OF UNILATERAL TRUNCATED RECONSTRUCTION

Sample	Projections	Size	Pitch	Magnification ratio	Offset (mm)	Turns
Simulation module	2160	512×512	1250	1.25	100	3
lithium battery	1440	957×991	1250	7.978	997	2

To assess the quality of the reconstructed images, normal spiral scanning is employed to acquire complete projection data. Subsequently, the projection images are artificially cropped to obtain truncated projection images. The complete projections are reconstructed using the spiral FDK algorithm, while the proposed method is utilized to reconstruct the truncated projection images. For the experiments conducted on real lithium batteries, the same conventional spiral scanning technique is employed to obtain complete projection data, and a control experimental group is generated using the same approach. The results of the control experiment are shown in Figs. 10 and 11.

From the comparative experiments of Figs. 10 and 11, it can be observed that the reconstructed images using the proposed algorithm for unilaterally truncated projections exhibit high quality, accurately preserving the details in the images. In order to quantitatively analyze the quality of the reconstructed images, the Peak Signal-to-Noise Ratio (PSNR), Structural Similarity Index Measure (SSIM), Mean Squared Error (MSE), Feature Similarity Index Measure (FSIM) and Visual Quality Fidelity (VIF) are computed for the images reconstructed based on the offset scanning data [11, 12], using the complete projection images reconstructed from real lithium battery data as the reference, as shown in Table III:

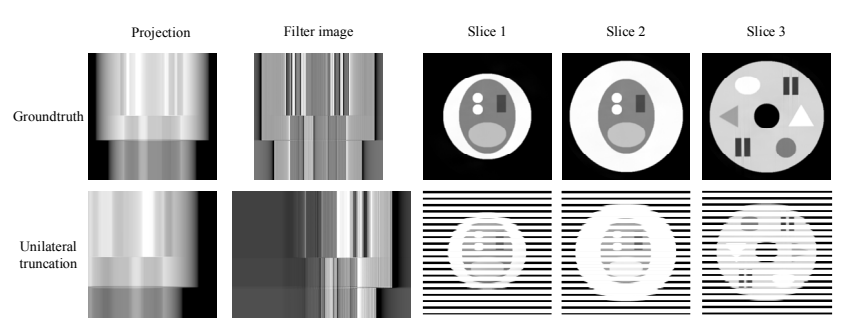


Fig. 10. Reconstruction of simulation data.

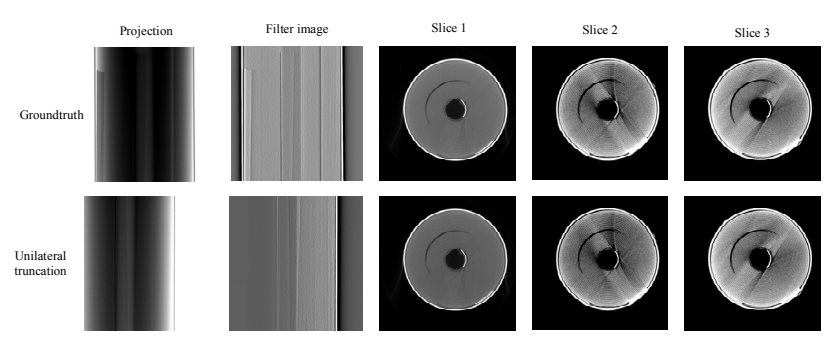


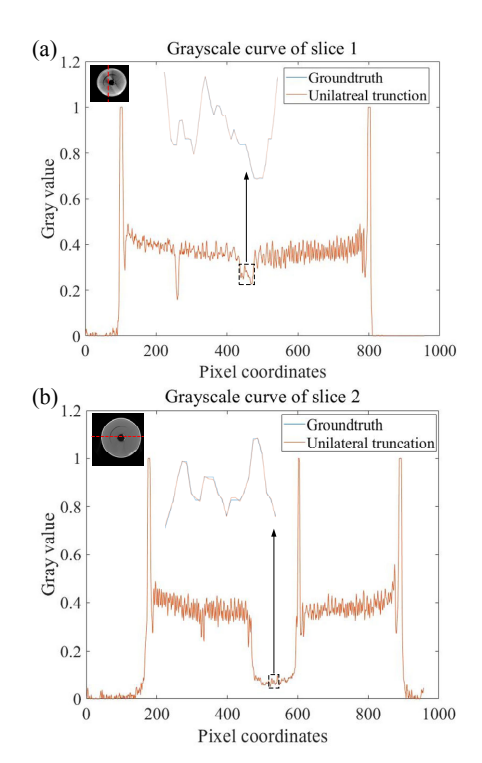
Fig. 11. Reconstruction of lithium battery data.

TABLE III. QUANTITATIVE ANALYSIS OF ALGORITHM PERFORMANCE

Slice	PSNR	SSIM	MSE	FSIM	VIF
1	32.471	0.9923	0.0123	0.9837	0.9711
2	33.774	0.9914	0.0095	0.9799	0.9687
3	33.323	0.9907	0.0139	0.9768	0.9693

From Table III, it can be observed that the reconstructed images exhibit a high similarity to the standard images. Particularly, the SSIM are all as high as 0.99, and the FSIM values are all above 0.975, indicating that the algorithm is capable of effectively recovering the details and structures of the images. All VIF scores exceed 0.965, demonstrating that the proposed algorithm expands the imaging field while preserving both fine details and structural integrity in the reconstructed images. Additionally, in order to

visually assess the similarity between the reconstructed and standard images, the grayscale curves are plotted for the three tomographic images separately, as shown in Fig. 12. It can be seen that the grayscale curves of the tomographic images reconstructed from the offset scans almost overlap with those reconstructed from the standard scans, thus validating the effectiveness of the proposed method.



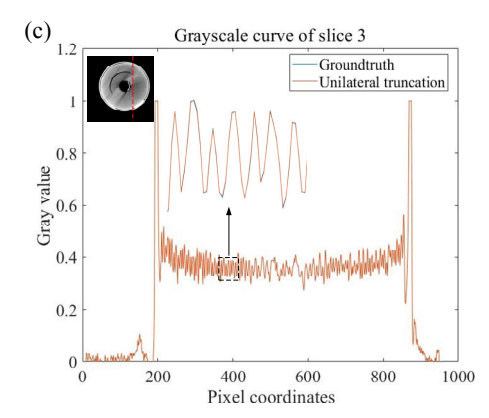


Fig. 12. Grayscale of lithium battery: (a) slice 1; (b) slice 2; (c) slice 3.

To enhance generality, authenticity, and credibility of the experiments, three additional sets of experiments are designed in this study, resulting in the acquisition of three sets of real offset spiral data. During the experiments, the sample coverage within the detector's FOV is achieved by horizontally moving the turntable, ensuring that only a portion of the area is covered. The specific parameters of the experiments are shown in Table IV:

TABLE IV. MAIN PARAMETERS OF GENERAL EXPERIMENTS

Sample	Projections	Size	Pitch	Magnification ratio	Offset	Turns
1	1440	484×1024	203.67	1.358	115	2
2	2160	623×1023	270.25	2.162	155	3
3	1440	775×945	1004.92	7.178	130	2

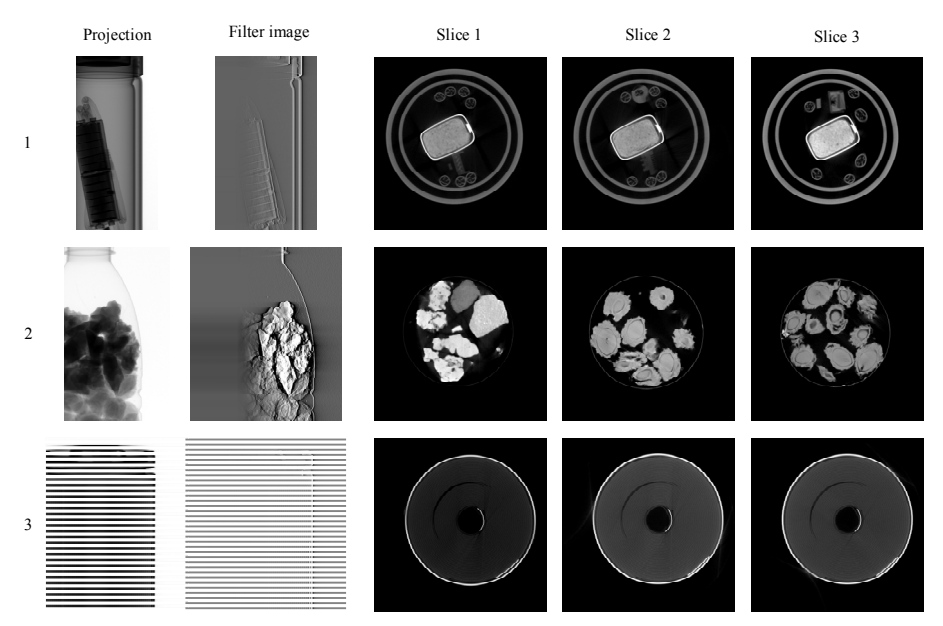


Fig. 13. Reconstruction of supplementary experimental data.

TABLE V. QUANTITATIVE ANALYSIS OF ALGORITHM PERFORMANCE

Sample	Slice	PSNR	SSIM	MSE	FSIM	VIF
	1	35.439	0.9936	0.0083	0.9866	0.9743
1	2	35.174	0.9921	0.0114	0.9812	0.9719
	3	35.787	0.9929	0.0093	0.9839	0.9742
	1	32.689	0.9907	0.0152	0.9724	0.9684
2	2	33.264	0.9930	0.0171	0.9773	0.9691
	3	33.812	0.9925	0.0087	0.9811	0.9718
	1	33.687	0.9919	0.0157	0.9874	0.9783
3	2	34.224	0.9923	0.0101	0.9835	0.9737
	3	34.311	0.9905	0.0176	0.9858	0.9759

As shown in Fig. 13, Sample 1 consists of a glass cup and a square lithium battery placed inside it; Sample 2 is composed of pebbles and dehydrated ginkgo fruits; Sample 3 is a lithium battery. It can be observed that the image reconstructed by the spiral FDK algorithm based on Parker weighting exhibits no apparent artifacts, and the image has high clarity and contrast. From the quantitative analysis in Table V, it can be seen that the proposed method can effectively reconstruct the details and structure of the image, and the image exhibits a high signal-to-noise ratio and similarity.

B. Additional Algorithm Complexity

The proposed algorithm aims to expand the imaging field of view while preserving image quality. Compared to the traditional FDK algorithm, it introduces additional algorithmic complexity. The extra algorithmic complexity—or computation time—introduced by the proposed method relative to a conventional FDK reconstruction comes from two sources:

- Parker weighting: this stage adds an additional processing pass over the projections, thus increasing runtime.
- Larger reconstruction grid: with the same projection width W, a large-FOV reconstruction must cover a wider slice because of the lateral offset. If the rotation-axis offset is Cor, the slice size becomes $(W + Cor) \times (W + Cor)$, whereas standard FDK produces only a $W \times W$ image.

For the Parker-weighting pass, Table VI shows the processing times measured for several data sets with different image sizes and frame counts. The increase in computational complexity for the reconstruction step is given by the formula (8):

TABLE VI. TIME SPENT ON IMAGES OF DIFFERENT SIZES AND QUANTITIES

Size	Frames	Time /ms
	500	613.94
512×512	1000	1189.27
	2000	2335.13
	500	2105.56
1024×1024	1000	4089.87
	2000	8112.91
	500	8227.38
2048×2048	1000	15,988.27
	2000	31,475.36

$$AddCmpty = (W + Cor)^{2} - W^{2} = Cor^{2} + 2W \times Cor$$
 (8)

As the equation shows, the additional computational complexity in the reconstruction stage increases linearly with both the projection width and the magnitude of the turntable offset.

C. FOV Limitations

In a cone-beam CT system, the FOV is constrained not only by the detector size but also by the magnification used during imaging. As shown in Fig. 14, let the detector width be *DetecLen*, the source-to-detector distance *SOs*, and the source-to-rotation-center distance *SO*. Under these conditions, when the rotation stage is given a unilateral

(one-sided) offset, the maximum FOV—namely, the diameter *D* of the transverse circumscribed circle—satisfies the following Eqs. (9) and (10):

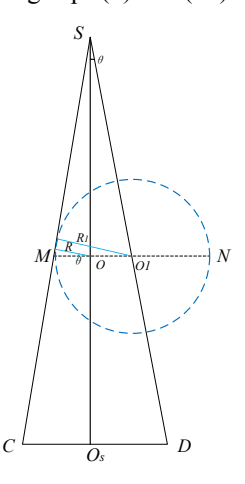


Fig. 14. Geometric diagram of cone beam CT system.

$$Ratio = \frac{\overline{SO}}{\overline{SO_s}}$$

$$\overline{MO} = \frac{\overline{CO_s}}{Ratio} = \frac{DetecLen}{2 \cdot Ratio}$$

$$\theta = arc \tan(\frac{DetecLen}{2 \cdot \overline{SO}})$$

$$R = \overline{MO} \cdot \cos \theta$$
(9)

$$D = 2 \cdot R_1 = 2 \left(R + \overline{OO_1} \cdot \frac{\overline{SO_S}}{\sqrt{\overline{O_S D}^2 + \overline{SO_S}^2}} \right)$$
 (10)

From Eq. (2), it can be concluded that as the magnification factor increases, the field of view decreases proportionally. In practical industrial CT inspection tasks, for large-sized workpieces with low spatial resolution requirements, it is recommended to position the object closer to the detector during scanning to reduce the magnification factor and expand the imaging field of view.

V. CONCLUSION AND DISCUSSION

In response to the problem of limited transverse FOV in high magnification conditions, this study expands the imaging FOV along the transverse direction by combining spiral scanning and offset scanning methods without changing the hardware configuration of the imaging system. By analyzing the symmetry of the projection images acquired over 360 degrees, the detector's imaging FOV can be extended up to twice its maximum size using Parker weights, while obtaining reconstruction image quality comparable to standard under projection truncation.

CONFLICT OF INTEREST

The authors declare no conflict of interest.

AUTHOR CONTRIBUTIONS

Dalong Tan designed the algorithm and conducted the

experiments; Xin Tian improved the algorithm and optimized the experiments; Yixin He and Chenhao Xu processed and organized the data; Kaisheng Li wrote the first draft of the paper; Min Yang revised the paper and provided guidance on the experiments.; all authors had approved the final version.

REFERENCE

- H. K. Lee, J. Fox, W. Tucker et al., "Simulation study to develop an X-ray source for stationary CT for realtime 4D imaging," Transactions of the American Nuclear Society, vol. 126, pp. 238– 240, 2022.
- [2] M. Hojjat, T. Ali, and A. Mojtaba, "Detection performance of pixelated Lutetium-Yttrium Oxyorthosilicate (LYSO) scintillators for high-resolution photon-counting CT imaging," *Review of Scientific Instruments*, vol. 94, no. 2, 023308, 2023.
- [3] S. Zhang and Y. Xia, "CT image reconstruction algorithms: A comprehensive survey," *John Wiley & Sons, Ltd*, vol. 33, no. 8, e5506 2021
- [4] P. R. Costa and E. C. A. Araujo, "Application of the FDK algorithm for multi-slice tomographic image reconstruction," *Revista Brasileira de Engenharia Biomédica*, vol. 26, no. 2, pp. 105–120, 2010
- [5] J. L. Chen and P. X. Yua, "Improvement of cone-beam FDK back projection reconstruction algorithm," *Practice and Understanding* of *Mathematics*, vol. 52, no. 6, p. 10, 2022.

- [6] X. Yan and R. M. Leahy, "Cone beam tomography with circular, elliptical and spiral orbits," *Phys. Med. Biol.*, vol. 37, no. 3, p. 493, 1992.
- [7] W. Bo, X. Ying, and H. T. Yu, "Two analytical reconstruction algorithms for spiral cone-beam computerized tomography," *Journal of Applied Optics*, vol. 32, no. 5, pp. 894–898, 2011.
- [8] H. Miao, "Study on an improved helical CB FDK algorithm," Journal of Sanming University, vol. 27, no. 04, pp. 335–349, 2010.
- [9] H. Z. Liang, "Improvements of FDK-type helical cone-beam CT imaging," Doctoral dissertation, Nanyang Technological University, pp. 19–22, 2007. https://dr.ntu.edu.sg/entities/publication/e23d24d 2-a457-4e64-b8e6-97118e7b2c4f
- [10] K. Jan, R. Ludwig, and K. Michael et al., "The rotate-plus-shift Carm trajectory. Part II. Exact reconstruction from less than 180° rotation," Medical Physics, vol. 43, no. 5, 2016.
- [11] Y. Al-Najjar, "Comparative analysis of image quality assessment metrics: MSE, PSNR, SSIM and FSIM," *International Journal of Science and Research (IJSR)*, vol. 13, pp. 110–114, 2024.
- [12] K. Ohashi, Y. Nagatani, and M. Yoshigoe et al., "Applicability evaluation of full-reference image quality assessment methods for computed tomography images," *Journal of Digital Imaging*, vol. 36, no. 6, pp. 2623–2634, 2023.

Copyright © 2025 by the authors. This is an open access article distributed under the Creative Commons Attribution License (CC-BY-4.0), which permits use, distribution and reproduction in any medium, provided that the article is properly cited, the use is non-commercial and no modifications or adaptations are made.